PAN POLSKA AKADEMIA NAUK

METROLOGY AND MEASUREMENT SYSTEMS

Index 330930, ISSN 0860-8229

www.metrology.pg.gda.pl

M&MS

S-BAND AND KU-BAND SAR SYSTEM DEVELOPMENT FOR UAV-BASED APPLICATIONS

Piotr Kaniewski[1)], Wojciech Komorniczak[2)], Czesław Leśnik[1)], Jacek Cyrek[2)], Waldemar Susek[1)], Piotr Serafin[1)], Michał Łabowski[1)]

1) *Military University of Technology, Faculty of Electronics, Gen. W. Urbanowicza 2, 00-908 Warsaw, Poland* (✉ *piotr.kaniewski@wat.edu.pl*, +48 261 839 080, *czeslaw.lesnik@wat.edu.pl, waldemar.susek@wat.edu.pl, piotr.serafin@wat.edu.pl, michal.labowski@wat.edu.pl*)

2) *WB Electronics S.A., Poznańska 129/133, 05-580 Ożarów Mazowiecki* (*w.komorniczak@wb.com.pl, j.cyrek@wb.com.pl*)

Abstract

This paper describes a synthetic aperture radar system for tactical-level imagery intelligence installed on board an unmanned aerial vehicle. Selected results of its tests are provided. The system contains interchangeable S-band and Ku-band linear frequency-modulated, continuous wave radar sensors that were built within a frame of a research project named WATSAR, conducted by the Military University of Technology and WB Electronics S.A. One of several algorithms of radar image synthesis, implemented in the scope of the project, is described in this paper. The WATSAR system can create online and off-line radar images.

Keywords: unmanned aerial vehicle (UAV), synthetic aperture radar (SAR), Range–Doppler algorithm (RDA), imagery intelligence (IMINT) system.

1. Introduction

Radar imaging techniques, such as *synthetic aperture radar* (SAR), enable the acquisition of high-resolution terrain images, comparable with aerial photography, but images can also be captured in foggy, dusty, or low ambient light environments [1–3]. This makes them complementary to optical systems, which require better visibility conditions. Therefore, these images are especially useful in military operations, which are often carried out in reduced visibility conditions over the battlefield and must be performed both day and night. Many civilian applications, such as observations of forest fires, can also benefit from these unique features of SAR.

This paper describes an *unmanned aerial vehicle* (UAV)-based SAR system, named WATSAR, elaborated and manufactured by the Military University of Technology (Warsaw, Poland) and WB Electronics S.A. (Ożarów Mazowiecki, Poland) in the years 2012–2016. Its primary application is to tactical-level *imagery intelligence* (IMINT). Since manned airborne platforms are considerably expensive, the aim of the project team was to install the system on board a mini UAV called FlySar, which was built by Flytronic (Gliwice, Poland).

Article history: received on Jun. 25, 2018; accepted on Oct. 13, 2018; available online on Mar. 29, 2019, DOI: 10.24425/mms.2019.126326.

This paper is organized as follows. The structure of the system is presented in Section 2 and its main components are described in Sections 3–6. Selected results of the tests of the system are demonstrated in Section 7, whereas Section 8 contains concluding remarks.

2. System structure

The system, shown in Fig. 1, includes a part installed on board a UAV and a ground-based part. The on-board and ground-based parts exchange commands, status information, and radar and navigation data via a dedicated C-band radio link. Some of the most important elements of the on-board part, including the radar sensor and the navigation instruments, are visible in the payload compartment, shown in Fig. 2. The UAV and the elements of the ground-based part of the WATSAR system are presented in Fig. 3.

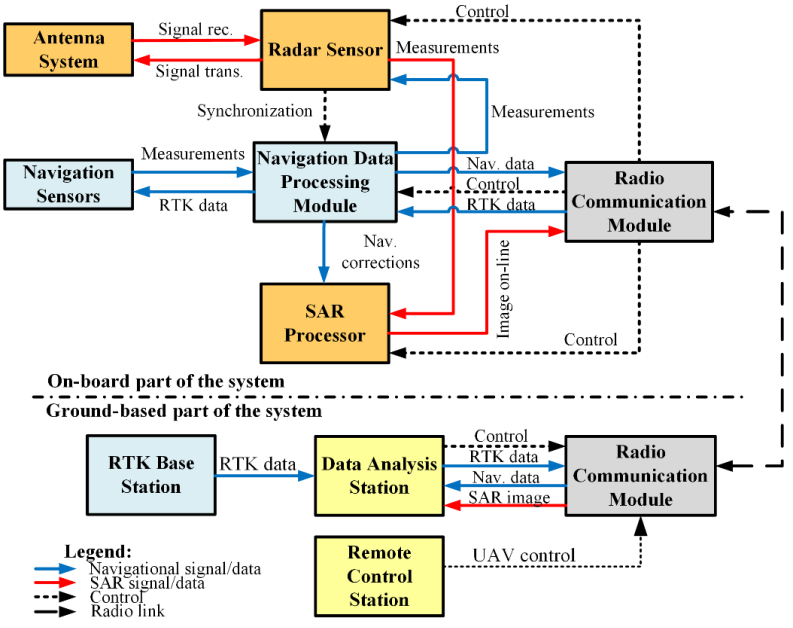

Fig. 1. A block diagram of the *unmanned aerial vehicle* (UAV)-based *synthetic aperture radar* (SAR) system.

The on-board part includes a transmitter/receiver module of the radar sensor with an antenna system and a data storage module, an on-board SAR processor, an integrated navigation system, and an on-board data transmission system. The system offers two levels of quality of the produced radar images. The received radar echo signals are stored in the data storage module for post-mission off-line synthesis of high-quality terrain images. At the same time, the signals are range-compressed and processed by the SAR processor to form lower resolution online SAR images. The resultant online images are transmitted to the ground-based station during UAV flight. The navigation system is mainly used to compensate for the adverse influence of the UAV flight instabilities on the quality of SAR images. The ground-based part includes a remote-control station and a data analysis station, which control the airborne part of the system and synthesize off-line radar images, respectively. The remote-control station sends its commands and receives data from the UAV with the use of a receiver/transmitter station.

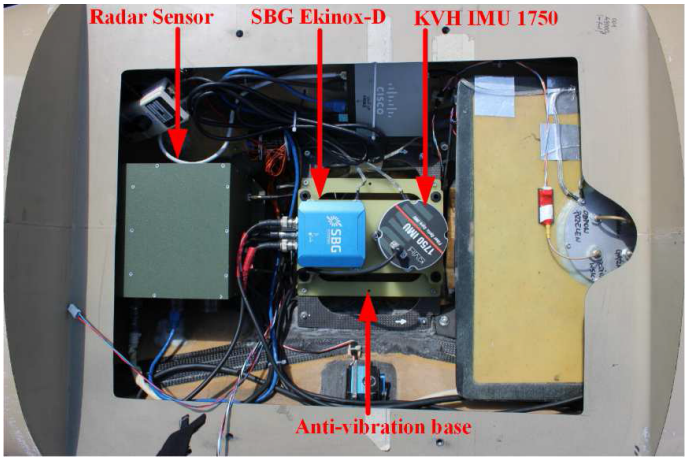

Fig. 2. A photo of radar sensor and navigation equipment of the UAV-based SAR system.

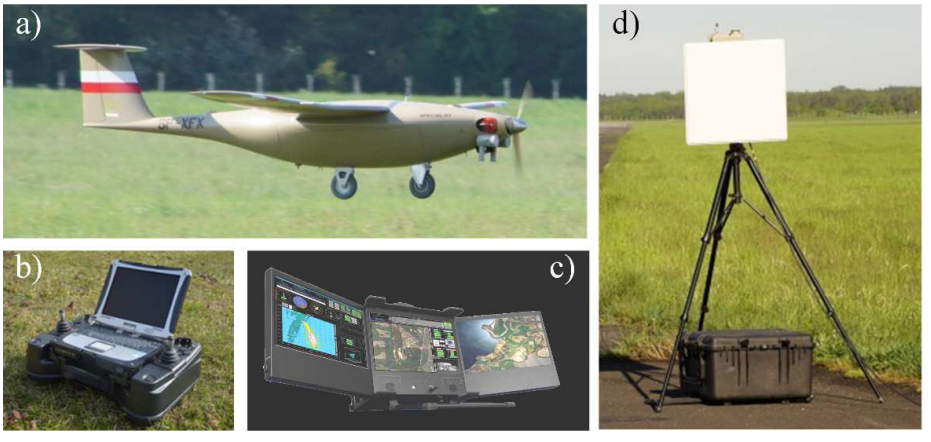

Fig. 3. Photos of WATSAR system: a) Mini-UAV designed and produced in WATSAR project; b) remote-control station; c) data analysis station and d) receiver/transmitter station.

3. Radar sensors and antenna system

During the project, two types of *linear frequency-modulated, continuous wave* (LFM-CW) radar sensors were developed for two different operating frequency bands: 2.91 GHz (S-band) and 15.9 GHz (Ku-band). Due to the greater wavelength, the SAR system with the S-band sensor is less sensitive to trajectory instabilities, but the use of the Ku-band sensor provides much better image resolution due to the wider band of the transmitted signal. The choice between the frequency bands is made by replacing one type of sensor with another, which can be easily and quickly performed in the field between two successive missions.

Block diagrams of S- and Ku-band sensors are shown in Fig. 4 and Fig. 5, respectively. Each sensor is composed of an FM-CW exciter and a microwave header. The exciter is responsible for generating the LFM-modulated sounding signal, processing the demodulated echo signals,

digitizing and storing them in the system memory as complex samples for off-line SAR image synthesis.

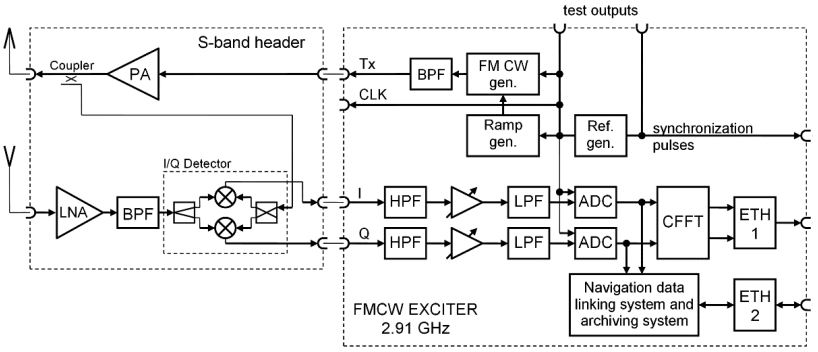

Fig. 4. A block diagram of the S-band radar sensor.

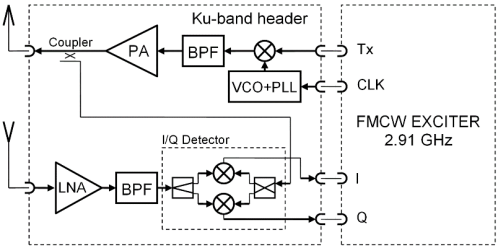

Fig. 5. A block diagram of the Ku-band radar sensor.

The microwave header [4] contains a power amplifier of the sounding signal and a receiver front-end with a quadrature demodulator of the echo signal. Additionally, the header of the Ku-band sensor contains an up-converter from 2.91 GHz to 15.9 GHz in its transmitting path.

The abbreviations used in Fig. 4 and Fig. 5 that were not previously explained in this paper are as follows: PA – *Power Amplifier*, LNA – *Low Noise Amplifier*, BPF – *Band Pass Filter*, HPF – *High Pass Filter*, LPF – *Low Pass Filter*, ADC – *Analog to Digital Converter*, CFFT – *Complex Fast Fourier Transform*, VCO – *Voltage Controlled Oscillator*, PLL – *Phase Locked Loop*, ETH – *Ethernet ports*.

The microwave header shown in Fig. 5 (Ku-band header), responsible for shifting the signal carrier frequency between 2.91 GHz and 15.9 GHz, is the most crucial and challenging component of the designed radar sensors. Block diagrams explaining its construction in more detail are presented in Fig. 6 (transmitting part) and Fig. 7 (receiving part). Both figures contain photos and symbols of the used microwave elements.

The transmitting part contains an up-converter with a triple-balanced mixer and a frequency synthesizer used as a local oscillator. The frequency range of the oscillator is 12.4 to 13.4 GHz. The following microwave components are used: (1) a triple-balanced mixer TB 0218 from Miteq; (2) a bandpass filter FI-15.9-400-10 from MCLI; (3) a frequency synthesizer HMC807LP6CE from Analog Devices; (4) two medium-power microwave amplifiers A2CP18615 from Teledyne; (5) a medium-power microwave amplifier A2CP18625 from Teledyne, and (6) a directional coupler C8-10 from MLCI.

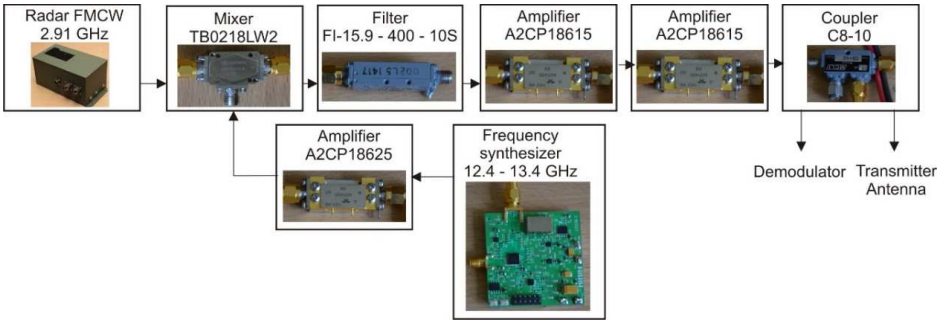

Fig. 6. A block diagram of the transmitting part of the Ku-band microwave header.

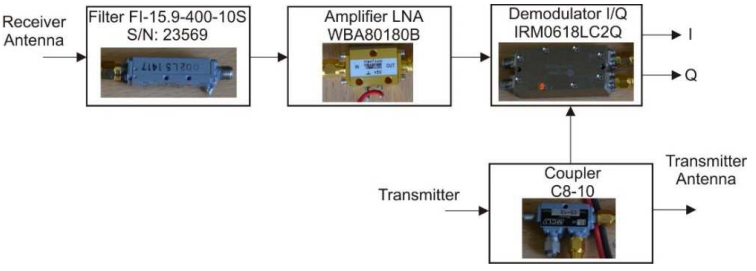

Fig. 7. A block diagram of the receiving part of the Ku-band microwave header.

The microwave amplifiers used in the transmitting part can be connected in a cascade without considering their excitation. This is possible due to the very small value of the S_{12} parameter of their scattering matrix.

The receiving part contains the following microwave components: (1) a bandpass filter FI-15.9-400-10S from MCLI, (2) a low-noise microwave amplifier WBA80180B from WanTcom, and (3) an I/Q demodulator IRM0218LC2Q from Miteq. The WBA80180B amplifier is a wideband microwave amplifier working in the frequency range of 8 to18 GHz with a gain of 35 dB and a noise factor equal to 2 dB.

To estimate the key parameters of the SAR system, the output *signal-to-noise ratio* (SNR_{OUT}) was calculated. This calculation should consider the input *signal-to-noise ratio* (SNR_{IN}) as well as effects of two-dimensional (2D) signal processing, including azimuth and range compression [1, 5, 6]. These effects can be expressed in terms of the azimuth processing gain G_A and the range processing gain G_R, and the relationship between the output and input signal-to-noise ratios is as follows [3]:

$$SNR_{OUT} = 2G_A G_R SNR_{IN}\,, \tag{1}$$

$$G_A = \frac{\Theta_a R}{2vT_i}\,, \tag{2}$$

$$G_R = BT_i\,, \tag{3}$$

where: Θ_a is the antenna beam width in the azimuth direction, R is the horizontal range to the object, v is the velocity of the UAV, T_i is the LFM ramp modulation time, and B is the bandwidth of the sounding signal.

The expected input *signal-to-noise ratio* (SNR_{IN}) can be obtained from the radar range equation. The input SAR receiver signal power P_s is given by:

$$P_s = \frac{P_t G_t G_r \lambda^2 \sigma}{(4\pi)^3 R_s^4}, \tag{4}$$

where: P_t is the transmitted power, G_t is the transmitting antenna gain, G_r is the receiving antenna gain, λ is the wavelength, σ is the radar cross-section of the object, and R_s is the slant range to the object.

The radar cross-section σ for the SAR system is given by:

$$\sigma = \sigma_0 A_r, \tag{5}$$

where σ_0 is a surface scattering coefficient (its values can vary from −25 dB to 20 dB) and A_r is a surface resolution coefficient, defined as:

$$A_r = \Delta R \Delta a, \tag{6}$$

where ΔR is the horizontal range resolution and Δa is the azimuth resolution. Finally, (4) can be written as:

$$P_s = \frac{P_t G_t G_r \lambda^2 \sigma_0 \Delta R d}{2(4\pi)^3 R_s^4}, \tag{7}$$

where d is the physical antenna length in the azimuth direction and $d = 2\Delta a$.

The noise power at the input of the SAR receiver is expressed as:

$$P_N = k\left[T_A + 290\left(F_{LNA} L - 1\right)\right] B, \tag{8}$$

where: k is the Boltzmann constant, T_A is the antenna noise temperature, F_{LNA} is the noise figure of the microwave amplifier, and L is the antenna line losses.

Substituting (7) and (8) into (1), the formulae can be obtained for $SNR_{OUT\,\min}$ and $SNR_{OUT\,\max}$, corresponding to $R_{s\,\max}$ and $R_{s\,\min}$, respectively, which are the distances to the closest and farthest objects illuminated by the antenna main beam, respectively:

$$\begin{aligned} SNR_{OUT\,\min} &= 2G_A(R_{s\,\max}) G_R \frac{P_t G_t G_r \lambda^2 \sigma_{0\,\min} \Delta R_{\max} d}{2k\left[T_A + 290\left(F_{LNA} L - 1\right)\right](4\pi)^3 R_{s\,\max}^4} \\ SNR_{OUT\,\max} &= 2G_A(R_{s\,\min}) G_R \frac{P_t G_t G_r \lambda^2 \sigma_{0\,\max} \Delta R_{\min} d}{2k\left[T_A + 290\left(F_{LNA} L - 1\right)\right](4\pi)^3 R_{s\,\min}^4} \end{aligned}, \tag{9}$$

where $\Delta R_{\min}$ and $\Delta R_{\max}$ are the horizontal range resolution values at the distances $R_{\min}$ and $R_{\max}$, respectively.

Equation (9) enables to calculate the following parameters: the dynamic range of A/D converters or the required transmitted power for assumed parameters of the SAR system, such as a required SNR_{OUT}, the period of the LFM signal, the bandwidth of the sounding signal, the antennas' parameters, and velocity and altitude of the flight of the UAV. The main parameters of both S-band and Ku-band radar sensors are provided in Table 1.

Dedicated patch antenna systems were developed for each frequency band. The 2.91 GHz antenna is a 2D in-phase radiator array. The radiators are half-wave dipoles. The dipoles were placed on opposite sides of the substrate. A photo of the antenna is shown in Fig. 8.

Table 1. Comparison of parameters of S-band and Ku-band radar sensors.

Parameter	Symbol	Unit	Radar Sensor	
			S-band	Ku-band
Centre frequency	f_0	GHz	2.91	15.9
Sounding signal bandwidth	B	MHz	100	184
LFM ramp modulation time	T_i	ms	1	1
LFM ramp repetition frequency	F_P	Hz	826	826
Power transmitter	P_t	dBm	+20	+20
Power transmitter balance	ΔP_t	dBm	±1	±1
Linearity LFM	$\Delta f/B$	–	4×10^{-4}	4×10^{-4}

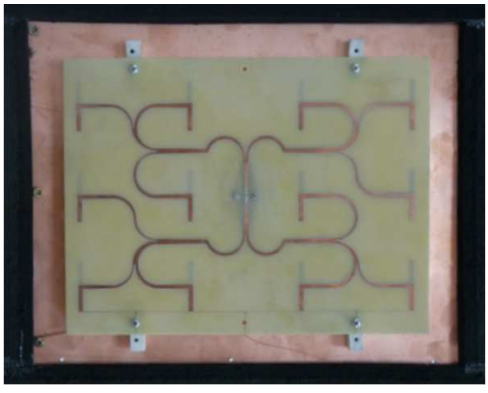

Fig. 8. A photo of the 2.91 GHz antenna with a reflector.

The 15.9 GHz antenna was designed as a microstrip 4×6 array. It is powered by a power distribution system implemented using Wilkinson and T dividers. Details of the antenna construction are shown in Fig. 9.

a) b)

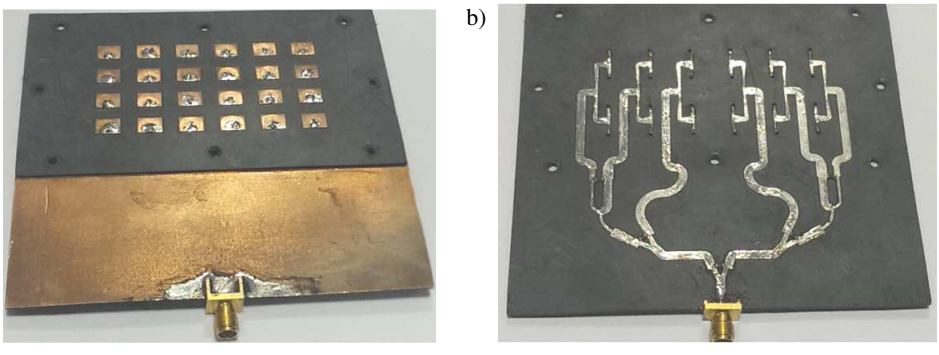

Fig. 9. Photos of the 15.9 GHz antenna: a) from the side of radiators; b) from the side of the power distribution system.

In Table 2, a comparison of the measured main parameters of the two antenna system types is presented.

Table 2. Comparison of main parameters of the S-band and the Ku-band antennas.

Parameter	Unit	Antenna system	
		S-band	Ku-band
Center frequency	GHz	2.91	15.9
Bandwidth	MHz	400	$2 \cdot 250$
Beam-width in H-plane	degrees	19.0	14.0
Beam-width in E-plane	degrees	29.0	28.0
Side lobe level in H-plane	dB	−15.0	−11.0
Side lobe level in E-plane	dB	−20.0	−13.0
Gain	dBi	15.8	13.8

4. Image synthesis algorithm

Due to the instability of the trajectory of the UAV platform, a modified version of the *Range–Doppler Algorithm* (RDA) [1, 5] was implemented in the system. The modifications enable to apply navigation corrections that describe the deviations of the actual platform trajectory from the assumed ideal trajectory. The corrections are computed by the navigation system and are used in the SAR algorithm to compensate for echo signals' phase changes resulting from the instabilities.

The RDA enables to obtain the SAR image much faster than time-domain algorithms, but implementing the platform motion compensation in the RDA is much more difficult. This is because the RDA computes the image for several range lines at a time with the same reference function.

In order to consider the navigation corrections along the trajectory, the modified Range–Doppler Algorithm divides the acquisition session into smaller parts in which the corrections may be assumed constant, and creates SAR sub-images.

The width of a sub-image does not need to be correlated with the size of the *synthetic aperture* (SA); however, the trajectory associated with a sub-image must be longer than the width of the corresponding sub-image by the SA length. A simplified block diagram of the modified RDA is shown in Fig. 10.

In the LFM-CW radar sensor the down-converted raw signal comprises a mixture of harmonic echo signals having frequencies dependent on the distance from the radar to the object.

The first step of the algorithm is the fast Fourier transform in the range direction, which plays a role of the range compression in LFM-CW radar systems. The subsequent steps of the algorithm are performed for each of the sub-images separately. In the next step, the range-compressed signal is transformed to the Doppler frequency domain (along the azimuth dimension) and the Range Cell Migration Compensation procedure is performed. Simultaneously the reference function of the SAR system is compensated for the motion errors computed for the centre of the synthetic aperture. After that the azimuth compression procedure is executed as the fast convolution (multiplication of spectra) of the raw signal and the motion-compensated reference function. The product of the two spectra is transformed to the time domain, therefore the algorithm of computing each of the sub-images may be described as follows:

$$G(p,q) = FFT_A^{-1}\left\{FFT_A\left[s_R(m,n)\right] FFT_A\left[\left(f_{refMC}(m)\right)\right]\right\}, \tag{10}$$

where FFT_A and FFT_A^{-1} represent the fast Fourier transform and the inverse fast Fourier transform in the azimuth direction, respectively; $s_R(m,n)$ is the down-converted and range-compressed raw SAR signal; and $f_{refMC}(m)$ is the motion-compensated SAR reference function.

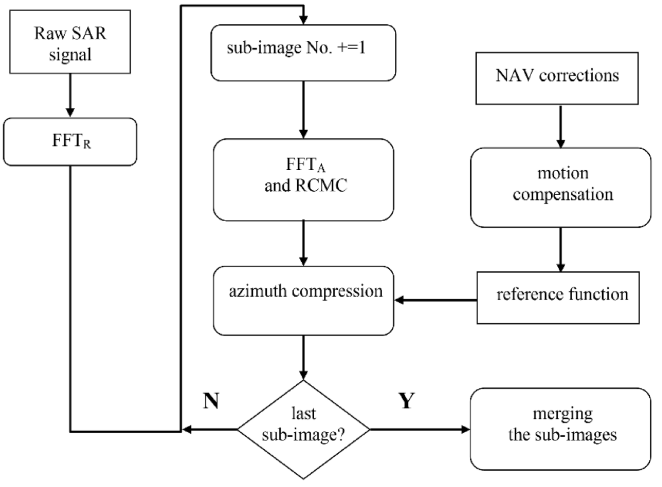

Fig. 10. A simplified block diagram of the modified Range–Doppler Algorithm.

The direct and inverse Fourier transforms were computed with the algorithms included in the library functions provided by the development environment that was used for implementing the system.

5. Integrated navigation system

Due to the small dimensions of the platform, its interaction with the atmosphere leads to unfavourable UAV position and velocity changes that modulate the received echo signal and cause mismatch between the signal and the assumed reference function. The on-board integrated navigation system (Fig. 11) was elaborated to calculate navigational corrections for the online and off-line SAR image synthesis algorithms, where they were used to correct the phases of the echo signal. The corrections represent estimated differences between the real and the assumed UAV positions and its velocity along a presumed rectilinear trajectory. The system includes a *navigation data processing module* (NDPM), an *inertial measurement unit* (IMU) KVH 1750 and an INS/GNSS unit SBG Ekinox-D, capable of receiving *real-time kinematic* (RTK) corrections from the ground data analysis station. The algorithms implemented in the NDPM mainly include inertial navigation, Kalman filtering, and estimation of navigational corrections [8, 9]. Given the RTK corrections, the position of the UAV can be estimated with centimetre-level accuracy in the horizontal plane. In theory, in order to obtain a fully-focused SAR image, the position error should be less than a quarter of the wavelength (0.019 m); however, the achieved navigation results enable to obtain good-quality images with a relatively small computation effort in comparison with the autofocusing methods.

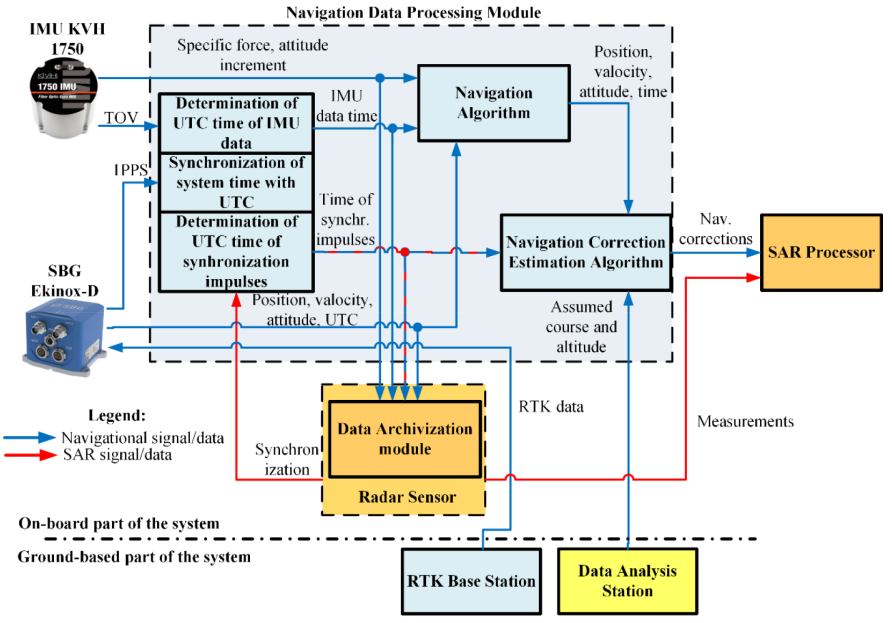

Fig. 11. A block diagram of the integrated navigation system.

6. Radio link and communication system

The exchange of data between the ground-based and on-board parts of the system is accomplished using a C-band radio link. The system is similar to the one used for communication with the mini-UAVs FlyEye (produced by WB Electronics) and currently used by the Polish Armed Forces. However, it was adopted to the new and larger FlySar platform by the UAV producer, Flytronic company.

Considering the demanding environment in which the UAV operates and the complexity of the propagation processes, *orthogonal frequency-division multiplexing* (OFDM) was implemented. To increase the operating range of the system, its ground station was equipped with an autonomous high-gain directional-antenna system, capable of tracking the UAV during flight. Adaptive allocation of power, based on the correlation between the distance from the ground station to the UAV and the noise level in the radio link, was applied to prolong the time of operation and increase the operating range of the system.

The main parameters of the radio link are presented in Table 3.

Table 3. Parameters of the radio link.

Parameter	Value
Frequency band	C
Mode	half duplex
Type of multiple access	TDMA
Transmission lags	< 100 ms
Operating range	≤ 30 km
Bitrate	≤ 30 Mbps

7. Results of trials

All the WATSAR system in-flight tests were performed at an airfield in Kamien Slaski, Poland. During the described tests, only the 15.9 GHz sensor was used.

A typical flight path of the UAV is shown in Fig. 12. The blue line represents a trajectory acquired from the INS; it is very smooth but diverges from the true trajectory along with the time of flight. The red line represents a more accurate trajectory from the INS/GNSS integrated navigation system. SAR images were synthesized mainly for quasi-rectilinear sections of stadium-shaped trajectories. The flight speed of the UAV was about 85 km/h.

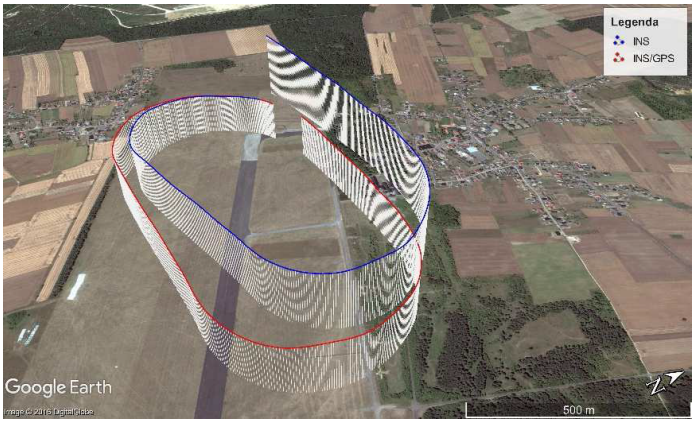

Fig. 12. A typical flight path of the UAV during tests.

The radar images obtained during various measurement campaigns have been presented in [7]. The SAR image in Fig. 13 was obtained with the 15.9 GHz sensor and computed with the modified RDA in the off-line mode. The presented image differs from the one presented in [7] as it was taken from a relatively high altitude of over 400 m and includes a larger urban area. Most other experiments were carried out during flights at altitudes between 150 and 300 m. Due to the greater distance to the observed area, the image synthesis algorithm required a longer synthetic aperture to maintain the assumed resolution. The obtained azimuth resolution of the image was about 80 cm and the range resolution was about 1 m.

a) b)

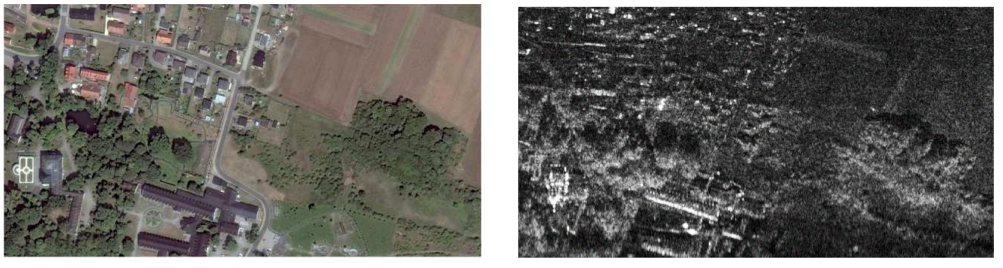

Fig. 13. a) An aerial photography and b) an SAR image of the south part of Kamien Slaski, Poland.

8. Conclusions

This paper presents a UAV-based SAR system, dedicated mainly for IMINT, its main algorithms, and selected results of its trials. The elements of the system, given its modular topology, can be enhanced separately, which makes the system flexible for future development. Currently, the main goal of the team is to reduce the system weight and size to enable its installation on even smaller platforms, such as FlyEye from WB Electronics. Further optimization of the image synthesis algorithms is also planned to improve the quality of the SAR images in the online operation mode.

Acknowledgements

This project was supported by the National Centre for Research and Development, Poland, in the frame of Applied Research Programme under Research Project PBS/B3/15/2012.

References

[1] Wang, B.C. (2008). *Digital Signal Processing Techniques and Applications in Radar Image Processing*, Hoboken & New Jersey: John Wiley & Sons Inc.

[2] Gromek, D., Samczynski, P., Kulpa, K., Cruz, G., Oliveira, T., Felix, L., Goncalves, P., Silva, C., Santos, A., Morgado, J. (2016). C-band SAR radar trials using UAV platform. *Proc. of the International Radar Symposium* (*IRS*), Krakow, Poland.

[3] Caris, M., Stanko, S., Essen, H., Leuther, A., Tessmann, A., Weber, R.; Malanowski, M., Samycznski, P., Kulpa, K., Meszoly, G., Topping, C., Georgiou, G., Papanastasiou, A., Guraly, R., Bilacz, Z. (2012). Synthetic aperture radar for all weather penetrating UAV application. *9th European Conference on Synthetic Aperture Radar*, Nuremberg, Germany, 290–293.

[4] Susek, W., Stec, B., Rećko C. (2011). Noise Radar with Microwave Correlation Receiver. *Acta Physica Polonica A*, 119(4), 483–487.

[5] Bamler, R. (1992). A comparison of Range–Doppler and wavenumber domain SAR focusing algorithms. *IEEE Transactions on Geoscience and Remote Sensing*, 30.

[6] Cumming, I., Wong, F. (2005). *Digital Processing of Synthetic Aperture Radar Data Algorithms and Implementation*, Boston & London: Artech House.

[7] Kaniewski, P., Komorniczak, W., Lesnik, C., Cyrek, J., Serafin, P., Labowski, M. (2016). Chosen results of field tests of synthetic aperture radar system installed on board UAV. *Proc. of SPIE: XI Conference on Reconnaissance and Electronic Warfare Systems*, Ołtarzew, Poland.

[8] Łabowski, M., Kaniewski, P., Serafin, P. (2016). Inertial Navigation System for Radar Terrain Imaging. *Proc. of IEEE/ION Position Location and Navigation Symposiu*m, Savannah, GA, USA, 942–948.

[9] Konatowski, S., Kaczmarek, B. (2009). Effectiveness of position estimating in nonlinear filtering approximation. *Przeglad Elektrotechniczny*, 85, 15–21.